

Multi-Attention Generative Adversarial Network for Remote Sensing Image Super-Resolution

Meng Xu, Zhihao Wang, Jiasong Zhu, Xiuping Jia, Sen Jia

Abstract—Image super-resolution (SR) methods can generate remote sensing images with high spatial resolution without increasing the cost, thereby providing a feasible way to acquire high-resolution remote sensing images, which are difficult to obtain due to the high cost of acquisition equipment and complex weather. Clearly, image super-resolution is a severe ill-posed problem. Fortunately, with the development of deep learning, the powerful fitting ability of deep neural networks has solved this problem to some extent. In this paper, we propose a network based on the generative adversarial network (GAN) to generate high resolution remote sensing images, named the multi-attention generative adversarial network (MA-GAN). We first designed a GAN-based framework for the image SR task. The core to accomplishing the SR task is the image generator with post-upsampling that we designed. The main body of the generator contains two blocks; one is the pyramidal convolution in the residual-dense block (PCRDB), and the other is the attention-based upsample (AUP) block. The attentioned pyramidal convolution (AttPCConv) in the PCRDB block is a module that combines multi-scale convolution and channel attention to automatically learn and adjust the scaling of the residuals for better results. The AUP block is a module that combines pixel attention (PA) to perform arbitrary multiples of upsampling. These two blocks work together to help generate better quality images. For the loss function, we design a loss function based on pixel loss and introduce both adversarial loss and feature loss to guide the generator learning. We have compared our method with several state-of-the-art methods on a remote sensing scene image dataset, and the experimental results consistently demonstrate the effectiveness of the proposed MA-GAN.

Index Terms—Super-resolution (SR), Multi-attention, Generative adversarial nets (GANs), Remote sensing image

I. INTRODUCTION

Image super-resolution (SR) is a rapidly growing issue in computer vision and has received considerable critical attention in recent years. Image SR aims to recover high-resolution (HR) images from given low-resolution (LR) images. It is essential for a wide range of real-world applications such as medical image processing [1]–[3], compressed image/video enhancement [4], [5], surveillance and security [6], [7], etc. Image super-resolution is not only about improving the visual quality of images: more importantly, almost all vision tasks can benefit from it. HR images generated by SR methods offer more options for vision tasks because they contain richer information.

As for the field of remote sensing, image super-resolution is even more significant. SR methods can facilitate other remote sensing missions, such as target detection [8]–[10], environmental monitoring [11]–[13], scene analysis [14] and so on. It is common knowledge that remote sensing images are generally acquired by satellites from high altitude. This

results in the low spatial resolution of remote sensing images. The quality of remote sensing images is also affected by many factors, such as motion blur, atmospheric interference (e.g., cloud cover), ultra-long-range imaging, transmission noise, etc. [15], [16]. Some of these problems can be solved by utilizing more advanced equipment, but this equipment is more expensive with respect to both launch deployment and routine maintenance. It is therefore easy to conclude that the most appropriate way to obtain high-resolution images is through SR algorithms.

Unfortunately, image super-resolution is a severely ill-posed problem, as the process of image degradation is not unique and there is therefore no certain solution. Traditional image super-resolution algorithms are basically interpolation-based or reconstruction-based. Interpolation-based methods obtain a pixel value by using its neighborhood information, and interpolation algorithms such as linear and bicubic [17] interpolation and lanczos [18] upsampling are essentially different with respect to neighborhood selection and calculation methods. Although interpolation-based methods are less computationally demanding, they often fail to recover the high-frequency information and therefore result in an excessively smooth image with blurred details, especially edges and texture information. For reconstruction-based SR algorithms, they achieve better results by using different prior knowledge or constraints in the form of distribution or energy function between HR and LR images. Local [19], [20], nonlocal [21] and sparse priors [22], [23] are the most widely used constraints for image super-resolution tasks. Reconstruction-based methods mostly use singular prior knowledge or a combination of several instances of prior knowledge. However, in comparison to methods based on interpolation, they are more computationally demanding. Meanwhile, these manually designed priors may not perform well when the scene changes.

Recently, with the development of machine learning (ML), learning-based SR algorithms have emerged. These algorithms attempt to establish an implicit mapping from LR images to the corresponding HR images through ML models. Among these algorithms, there has been a huge explosion in the number of deep learning (DL)-based SR algorithms. In this paper, we only focus on DL-based SR algorithms. Since Dong et al. proposed SRCNN [24] in 2014, an increasing number of studies have been performed by using convolutional neural networks (CNNs) for SR tasks, due to the powerful non-linear fitting and learning capabilities of CNNs. At the same time, with the development of several excellent CNNs (ResNet [25], DenseNet [26], etc.), more CNN-based SR networks have emerged, such as VDSR [27], EDSR [28], DBPN [29] and

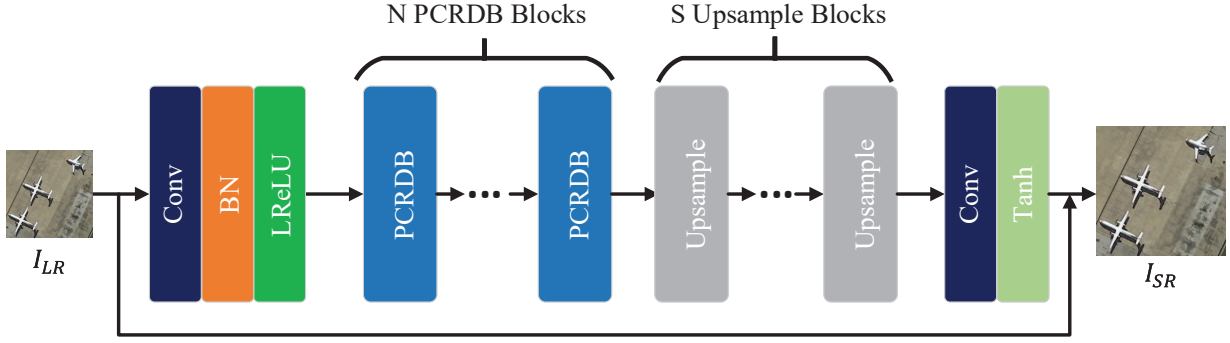


Fig. 1. Architecture of the MA-GAN generator.

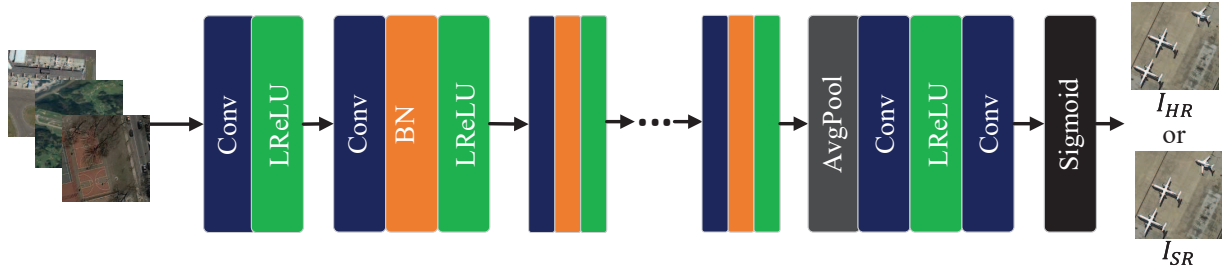


Fig. 2. Architecture of the MA-GAN discriminator.

others. These end-to-end models need to be trained with a large number of paired LR and HR images to learn the mapping from LR to HR images. Thanks to the advancement of DL, these models can use deeper and more complex networks to learn higher-level features and thus produce higher-quality HR images. Although CNN-based SR algorithms outperform the others, remote sensing images are somehow different from natural images. Compared with natural images, the target in a remote sensing image covers fewer pixels and the background is more complex. For example, a desert image may contain less textures, but a dense residential area will contain an extremely rich amount of textural information, making super-resolution of remote sensing images more difficult. The current work [15], [30] already addresses some of these issues to some extent.

In this work, we proposed a GAN [31]-based SR network that increases the resolution for remote sensing images in a satisfactory way, which is called the multi-attention super-resolution network (MA-GAN), as shown in Figure 1 and Figure 2. The main body of the generator, which is the core of the super-resolution task, consists of two modules; one is the PCRDB block (Figure 3), and the other is the AUP block (Figure 4(b)). The structure of the PCRDB block is similar to that of ESRGAN [32], which includes skip [25] and dense [26] connections to better extract features. However, we replace the last convolution operation with an AttPConv of our own design. The AttPConv block first performs multi-scale convolution without requiring more computations, and subsequently computes channel attention [33] on the feature maps obtained after convolution at different scales in order to dynamically adjust each feature map to achieve better SR performance. Compared with ESRGAN, which uses a fixed

parameter (which needs to be designed manually) to scale the residuals, our PCRDB undoubtedly makes more full use of the powerful learning ability of CNNs and is more generalizable. The AUP block is a module that can upsample the input feature map by an arbitrary multiple. It first upsamples the input by nearest neighbor interpolation and then fine-tunes the result of the upsampling by means of a small neural network and PA [34]. Since simple upsampling can lead to excessively smooth output, the design of the AUP block can compensate for the drawbacks caused by interpolation and thus enable better SR results.

In summary, the contributions of this work are as follows:

1. First, we proposed a GAN-based SR network that offers the ability of increasing the resolution for remote sensing images with any scale factor. Our experiments on the NWPU-RESISC45 dataset demonstrate that the performance of the proposed MA-GAN approach outperforms the state-of-the-art SR methods.
2. We design the PCRDB block that contains AttPConv. PCRDB extracts features better by skip and dense connections, and features at different scales can be obtained by multi-scale convolution in the final AttPConv block, and then the residuals can be adjusted for each feature map by the final channel attention.
3. We design the AUP block. With its nearest neighbor interpolation at the beginning, the AUP can achieve up-sampling at any scale. The small CNN and PA immediately after interpolation can be adjusted based on the interpolated feature maps to achieve better upsampling results.

The remainder of this paper is organized as follows. Section II briefly reviews the related works. Section III presents the

proposed MA-GAN in detail. Experimental results are shown in Section IV. Finally, the conclusion is presented in Section V.

II. RELATED WORK

A. Upsampling Method

The aim of image SR is to improve the resolution of the image, so the upsampling method is indispensable for any SR algorithm, and the way in which it is performed will also affect the final result. There are three commonly used upsampling methods. The first one is interpolation. The second is the subpixel convolution layer [35] proposed by Shi et al., which transforms the feature map $F_a \in \mathbb{R}^{h \times w \times r^2 c}$ into a new feature map $F_b \in \mathbb{R}^{r h \times r w \times c}$ by a scale factor of r (h, w and c are the height, width and channels of feature maps). The last upsampling method is transposed convolution, also called deconvolution in some papers. The most common approach to using transposed convolution is the up- and down-projection unit module proposed in the DBPN [29]. In recent studies, researchers have favored the direct use of interpolation for upsampling. This is because operations such as transposed convolution can introduce checkerboard-like artifacts that affect the experimental results, and subpixel and transposed convolution can only upsample integer multiples, which is more restrictive. In this paper, interpolated upsampling is used to achieve super-resolution at any scale factor.

B. Super-Resolution Framework

SR networks can be divided into four types, depending on where the upsampling operation is located in the network: pre-upsampling, post-upsampling, progressive upsampling, and iterative up and down sampling SR frameworks [29]. The pre-upsampling framework [24], [36] achieves the difficult upsampling task by interpolation at the beginning and later refines the interpolated image. The pre-upsampling framework is easier to train because only the coarsest images need to be refined, but it costs more time and space because of its higher-dimensional feature maps. The post-upsampling framework [28], [37] can be trained much more rapidly because it includes the upsampling step at the end. By dividing the upsampling into smaller tasks, the progressive upsampling framework [38] not only speeds up training but also yields better results. The iterative up and down sampling framework [15], [29] allows for better mining of the relationships between paired LR and HR images, but because of its complex framework and large number of up- and down-sampling operations, it often requires heavy manual network design.

C. Loss Function

The loss function is one of the most essential aspects in image SR tasks since one LR image could correspond to several HR images. A suitable loss function brings the generative model closer to the true HR image area in its latent space.

We denote I_{LR} for an LR image, I_{HR} for an HR image and I_{SR} for the generated HR image. Almost all SR algorithms

introduce a pixelwise loss that brings I_{SR} closer to I_{HR} in pixel value. L_1 loss and L_2 loss are the most frequently used pixelwise losses. The pixel-level loss improves the peak signal-to-noise ratio (PSNR) of I_{SR} , but results in loss of high-frequency information. Therefore, Lefig et al. [37] presented perceptual loss with respect to perceptually relevant characteristics. GAN-based models have adversarial loss, which helps the generator to produce higher quality images with the help of a discriminator. In addition to these losses, there are also texture losses [39], cycle consistency loss [40], etc.

III. PROPOSED MULTI-ATTENTION GENERATIVE ADVERSARIAL NETS

In this section, we will introduce the proposed MA-GAN in detail. First, we will present the overall framework of the GAN used in this paper. Second, we will introduce the multi-attention mechanism and describe each block in detail. Finally, we will present a description of the loss function used in this paper.

A. Network Framework

To be able to generate higher quality HR images, we design a multi-attention generative adversarial network. It contains a generator and discriminator as shown in Figure 1 and Figure 2, respectively.

To speed up the training, we design a generator which belongs to a post-upsampling framework. The generator network can be divided into four parts. The head of the generator is a Convolution-BatchNormalize-LeakyReLU block, while the body part consists of N PCRDB modules, followed by S upsampling blocks. Finally, the tail of the generator consists of the convolution-Tanh block. In this paper, we consider the SR task as an optimization task, so we perform pixel-level summation of the output of the tail with interpolated I_{LR} , which has the same spatial resolution of I_{HR} . Since all GANs are difficult to train, this operation reduces the difficulty of training and shortens the time consumption to obtain the desired model. The detailed architecture of the PCRBD and AUP blocks will be introduced in Section III-B and Section III-C.

The discriminator we use is the same as SRGAN [37], which mainly consists of a Convolution-BatchNormalize-LeakyReLU block. The generated image I_{SR} is fed into the discriminator together with I_{HR} to calculate adversarial loss to guide the generator training.

B. Pyramidal Convolution in Residual-Dense Block

To introduce PCRBD, we first present the AttPConv block. AttPConv is a special convolution combining multi-scale convolution and multi-channel attention. As shown in Figure 4(a), our proposed multi-scale convolution is not simply composed of multiple parallel conventional convolutions, and we prefer to call it pyramidal convolution. The pyramidal convolution is implemented internally by grouping convolution without increasing the computational cost or the model complexity [41]. The pyramid convolution in this paper has three different

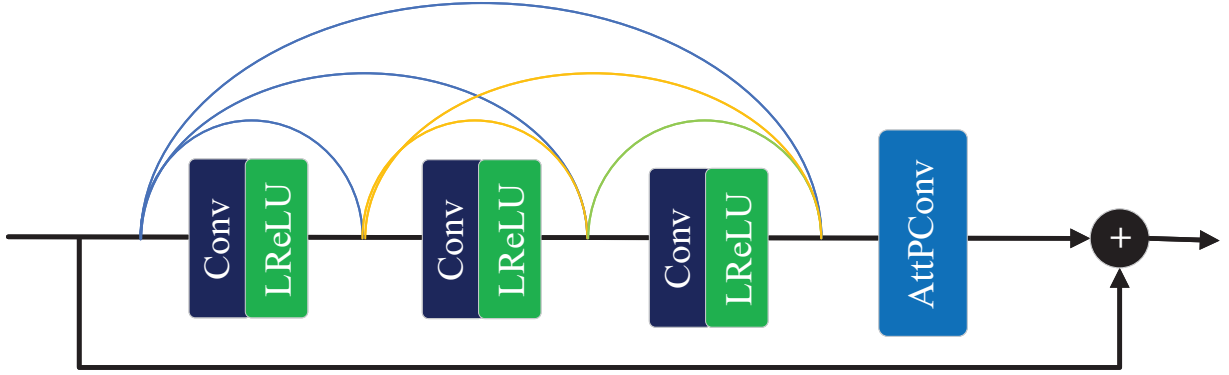


Fig. 3. The PCRBD Block.

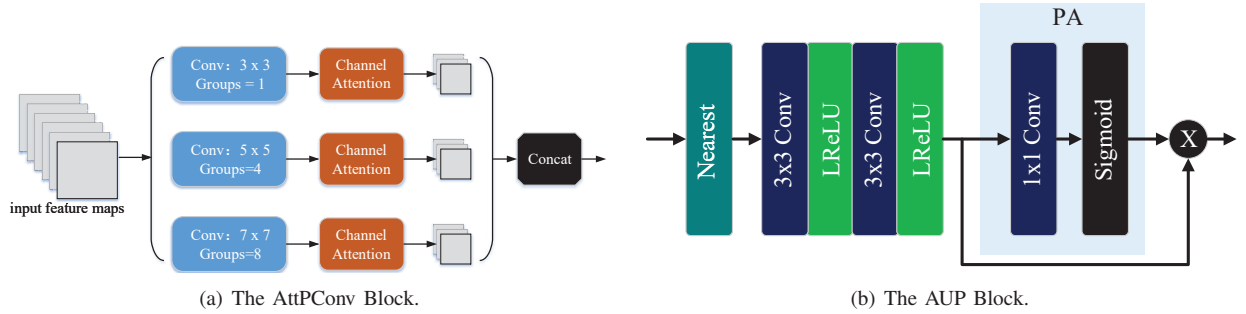


Fig. 4. Modules containing attention mechanisms

kernels, 3×3 , 5×5 and 7×7 , corresponding to the feature maps groups of 1, 4 and 8, respectively. Each group convolution is followed by a channel attention module [33], and all the feature maps are concatenated together as the final output. Based on this structure, the AttPConv block has the same input and output forms as the conventional convolution.

Since the AttPConv module contains an attention module, it is used as the last convolutional module of the PCRDB module. AttPConv follows 3 more Convolution-LeakyReLU modules, as shown in Figure 3. They are connected by dense connection [26]. The final output feature maps are obtained by element-level addition of the output of AttPConv and the input for the PCRDB module. It is worth mentioning that the residual-in-residual dense block (RRDB) proposed in ESRGAN has a structure similar to PCRDB. However, the RRDB block uses residual scaling [28], [42] to reduce the residuals by multiplying a constant between 0 and 1 before adding them to the main path to prevent instability. This constant can only be determined experimentally, which entails some additional work. We not only use convolution kernels of different size to extract feature information at different scales by the last AttPConv block in PCRDB. They also fulfill the role of scaling constant by channel attention, which is equivalent to multiplying a dynamic scaling constant, and this value is different for each feature map, thus scaling the residuals more accurately.

C. Attention-Based Upsample Block

We mentioned several upsampling methods in Section II-A, and since the subpixel convolution layer [35] and transposed convolution present some drawbacks, we use an interpolation-based upsampling method in this paper. However, simple interpolation can cause excessive smoothing of the image; thus, we design an upsampling module based on the pixel attention, as shown in Figure 4(b).

First, we perform nearest neighbor interpolation on the input of the upsampling module to improve the spatial resolution of the feature map. It is then fed into two Convolution-LeakyReLU blocks, and the feature map of the final Convolution-LeakyReLU block is denoted as $F_{up} \in \mathbb{R}^{h \times w \times c}$. The working process of the PA module can be described by the following Equation (1).

$$F_{PA} = Sigmoid(Con1 \times 1(F_{up})) \quad (1)$$

Here, F_{PA} refers to the output of the PA module and $Con1 \times 1$ represents the convolution operation with a kernel size of 1×1 . The channel number of the feature maps is reduced to 1 after $Con1 \times 1$, and then the $F_{PA} \in \mathbb{R}^{h \times w \times 1}$ is obtained after sigmoid operation. The values of F_{PA} are between 0 and 1 so that the feature map can be adjusted at the element level to produce better SR results.

D. Loss Function

In general, L_2 loss speeds up the training process, but it can introduce gradient explosion, and therefore the results are less

robust. L_1 loss has a stable gradient and is more robust, but in contrast, the training is slower and the solution is less stable. Since L_1 and L_2 losses both exhibit their own advantages and disadvantages, we choose smooth- L_1 loss, which combines the advantages of L_1 and L_2 losses, as the pixelwise loss. The smooth- L_1 loss is calculated as:

$$l_{pixel} = \begin{cases} 0.5 \times \frac{1}{r^2 HWC} \sum x^2 & \text{if } |x| < 1 \\ \frac{1}{r^2 HWC} \sum (|x| - 0.5) & \text{otherwise} \end{cases} \quad (2)$$

where $x = I_{HR} - I_{SR}$. H , W , and C are the height, width and channels of I_{LR} , respectively.

l_{pixel} makes the I_{SR} as close to the corresponding I_{HR} as possible at each pixel value to obtain high PSNR. However, this tends to ignore the high frequency information of the image and yield perceptually unsatisfying images. To solve this, inspired by the perceptual loss in SRGAN [37], we design the feature loss l_{fea} . The l_{fea} is based on the input for the last average pooling layer of the pretrained ResNet-18 [25] model. We denote the process of obtaining the desired feature map by $Extractor(\cdot)$. The feature loss l_{fea} is then defined as:

$$l_{fea} = \frac{1}{hwc} \sum [Extractor(I_{HR}) - Extractor(I_{SR})]^2 \quad (3)$$

We also introduced l_{adv} from the discriminator to assist in the training of the generator. The adversarial loss l_{adv} for G is:

$$l_{adv} = -\log(D(I_{SR})) = -\log(D(G(I_{LR}))) \quad (4)$$

where $G(\cdot)$ denotes the output of generator and $D(\cdot)$ denotes the output of discriminator.

The total loss for the generator is:

$$l_G = l_{pixel} + \alpha l_{adv} + \beta l_{fea} \quad (5)$$

where α and β are the weighting parameters for l_{adv} and l_{fea} , respectively.

For the discriminator, we use a loss function consistent with other GANs, shown as follows:

$$l_D = -\log(D(I_{HR})) - \log(1 - D(I_{SR})) \quad (6)$$

IV. EXPERIMENTAL RESULTS

A. Dataset

We perform experiments on the widely used remote sensing image dataset NWPU-RESISC45 [43]. This dataset contains a total of 31,500 images with 256×256 pixels covering 45 scenes. NWPU-RESISC45 contains large-scale remote sensing images that vary greatly in translation, spatial resolution, viewpoint, object pose, illumination, background, and occlusion. It also has high within-class diversity and between-class similarity. Therefore, it is a very challenging dataset for image SR. In this paper, we randomly divide the images of each of the scenes in the dataset into a training set, a validation set and a test set at a ratio of 8 : 1 : 1. All I_{HR} are resized to 224×224 in the experiments.

B. Implementation Details

We trained our network on a platform equipped with the Intel(R) Xeon(R) CPU (2.50 GHz) with 250-GB memory, an

TABLE I
THE DESCRIPTORS OF DIFFERENT SCENES.

No.	Scene	No.	Scene
S1	parking lot	S24	baseball diamond
S2	runway	S25	intersection
S3	island	S26	meadow
S4	sparse residential	S27	circular farmland
S5	commercial area	S28	basketball court
S6	terrace	S29	beach
S7	tennis court	S30	sea ice
S8	industrial area	S31	roundabout
S9	wetland	S32	dense residential
S10	desert	S33	chaparral
S11	stadium	S34	railway station
S12	overpass	S35	thermal power station
S13	snow berg	S36	harbor
S14	medium residential	S37	storage tank
S15	freeway	S38	forest
S16	ground track field	S39	railway
S17	church	S40	airport
S18	mobile home park	S41	palace
S19	lake	S42	ship
S20	rectangular farmland	S43	golf course
S21	mountain	S44	airplane
S22	bridge	S45	cloud
S23	river		

NVIDIA Tesla P100 with 16-GB memory and an AVAGO MR9361 with 2-TB capacity.

Our experiments used three scale factors: the simpler upsampling by a factor of 2, the more challenging upsampling by a factor of 4 and the more difficult upsampling by a factor of 8, which correspond with 4x, 16x, and 64x increases in image pixels, respectively. HR images I_{HR} are obtained from the divided dataset, then these images are downsampled by bicubic interpolation to obtain LR images I_{LR} , which represent the input for the generator, and all images are normalized to $[0, 1]$. The weighting parameter α for adversarial loss l_{adv} in Equation (5) is set to 10^{-3} and the weighting parameter β for feature loss l_{fea} is set to 10^{-2} .

The training process can be divided into two parts. We alternate between training the discriminator and the generator, first training the discriminator and then the generator. We first train the discriminator with l_D . The initial learning rate of discriminator lr_D is 0.0001. The lr_D is decreased by 1/2 when the training process is 25%, 50%, and 75% completed. We use Adam [44] with $\beta_1 = 0.5$, $\beta_2 = 0.999$ to optimize the discriminator. Whenever a training iteration of the discriminator is completed, a generator is trained with l_G immediately afterwards. The initial learning rate of generator lr_G is also set to 0.0001 and decreased by 1/2 when the training process is completed at 25%, 50%, and 75%. For the generator optimizer, we also use Adam [44] with $\beta_1 = 0.5$,

TABLE II
QUANTITATIVE COMPARISON OF MODELS USING DIFFERENT NUMBERS OF
PCRBD BLOCKS

Model	r	PSNR	SSIM
MA-GAN(3)	2	31.53	0.9007
	4	27.62	0.7640
	8	24.50	0.5429
MA-GAN(4)	2	31.97	0.9101
	4	27.76	0.7621
	8	24.54	0.5450
MA-GAN(5)	2	31.37	0.8959
	4	27.49	0.7442
	8	24.58	0.5409
MA-GAN(6)	2	30.99	0.8846
	4	27.96	0.7535
	8	23.85	0.5144
MA-GAN(7)	2	31.98	0.9102
	4	28.05	0.7520
	8	24.11	0.5245

$\beta_2 = 0.999$.

For the whole training process, we have carried out more than 10^6 update iterations both for the generator and the discriminator.

C. Evaluation using different numbers of PCRBD blocks

As for the image super-resolution task, the generator that produces the HR images is undoubtedly the most important part. The PCRBD block and AUP block, as the main body of the generator, serve very important roles in it. The number of AUP blocks S is determined by the scale factor r in the experiment. We set each AUP block to upsample by a scale factor of 2 so that S is 1, 2, and 3, corresponding to scale factors of 2, 4, and 8, respectively. Therefore, in this subsection, we conducted experiments on generators using different numbers of PCRBD blocks. We designed experiments with $N \in \{3, 4, 5, 6, 7\}$ for scale factors r of 2, 4, and 8, respectively. We denote the model containing N PCRBD blocks by MA-GAN(N). To be fair, the PSNR and structural similarity index measure (SSIM) are used as indicators for evaluating quantitative comparison. The quantitative experimental results are shown in Table II. We also produced a graph to compare the experimental results, shown in Figure 8.

When $r = 2$, MA-GAN(7) reaches the highest PSNR value of 31.98 dB. The lowest value of 30.99 dB corresponds with MA-GAN(4), a difference of 0.99 dB. Additionally, the SSIM values obtained for these two models are 0.9102 and 0.8846, respectively, with a difference of 0.0256. In regard to $r = 4$, MA-GAN(7) reaches the highest PSNR value of 28.05 dB. The lowest is MA-GAN(5) at 27.49 dB, a difference of 0.56 dB. The highest SSIM at this point is that of MA-GAN(3) at 0.7640, while the lowest is that of MA-GAN(5) at 0.7442, a difference of 0.0198. Finally, for $r = 8$, MA-GAN(5) obtained the highest PSNR value of 24.58 dB, while the lowest was

that of MA-GAN(6) at 23.85 dB, a difference of 0.73 dB. For SSIM, MA-GAN(4) obtained the highest value of 0.5450, and the lowest was that of MA-GAN(6) at 0.5144, a difference of 0.0306. It can also be more intuitively determined from Figure 8 that the performances of the different models do not differ much when N varies. This is due to our multi-attention mechanism, which allows the model to automatically adjust the input of the corresponding feature maps to achieve better SR performance.

D. Comparison with different methods

We further compare the performance of our MA-GAN with bicubic interpolation, and some advanced SR methods including SRCNN [24], FSRCNN [45], VDSR [27], EDSR [28] and DBPN [29], on the NWPU-RESISC45 [43] dataset. SRCNN, FSRCNN and VDSR are the three CNN-based networks that minimize the L_2 loss while EDSR and DBPN minimize L_1 loss. All of these methods are optimized on the same dataset and environment for a fair comparison.

In Section IV-C, we reach the conclusion that there is little difference in the performance of the models when N varies. Therefore, in this section, for each scale factor, we choose a better-performing MA-GAN. Specifically, for $r = 2$, we choose MA-GAN(7); for $r = 4$, we choose MA-GAN(3); and for $r = 8$, we choose MA-GAN(4).

Figures 5, 6, 7 show the visual comparisons between different SR methods when the scale factor $r = 2, 4, 8$, respectively. In these figures, we have selected only part of the I_{SR} for magnified display. The selected image area marked with red boxes is rich in texture information and is difficult to recover. In this way, we can observe the performances of different methods. In our experiments, EDSR did not successfully learn the mapping of LR images to HR images, and the results were less than satisfactory. From the figure, we can also determine that although our method can achieve the relative best results, there is still a gap between the I_{HR} and I_{SR} generated by our model, mainly the difficulty of recovering those tiny textural features.

Tables III, IV, and V show the quantitative comparisons when the scale factor $r = 2, 4, 8$, respectively. We have compared the super-resolution performances of the different models for each of the image scenes in the NWPU-RESISC45 dataset to obtain a more detailed comparison. The highest PSNR values for each scene are marked in red, and the highest SSIM is marked in blue.

For $r = 2$ (Table III), MA-GAN(7) obtains an average PSNR of 31.98 dB and an average SSIM of 0.9102, both of which rank first among all the methods. The PSNR of MA-GAN(7) is 1.43 dB higher than the second-best value, while the SSIM is 0.0005 higher. In terms of PSNR, MA-GAN(7) outperforms almost all of the scenes and is ranked first in SSIM for nearly half of the scenes. With $r = 4$ (Table IV), MA-GAN(3) performs best with an average PSNR of 27.62 dB and an average SSIM of 0.7640. The PSNR of MA-GAN(3) is 1.18 dB higher than the second-best value, while the SSIM is 0.0044 higher. The PSNR value of MA-GAN(3) is lower than those of the other comparison methods in 7 scenes. It

TABLE III
 QUANTITATIVE COMPARISON OF THE DIFFERENT SR METHODS ON THE DATASET (SCALE FACTOR $r=2$).

Scene	Bicubic		SRCNN		FSRCNN		VDSR		EDSR		DBPN		MA-GAN(7)	
	PSNR	SSIM	PSNR	SSIM	PSNR	SSIM	PSNR	SSIM	PSNR	SSIM	PSNR	SSIM	PSNR	SSIM
S1	25.27	0.8338	25.07	0.8400	24.69	0.8354	25.20	0.8657	21.57	0.6381	25.38	0.8635	27.61	0.8613
S2	33.36	0.9207	33.06	0.9194	32.17	0.9182	33.65	0.9385	27.06	0.8300	33.60	0.9377	34.11	0.9253
S3	38.57	0.9585	36.33	0.9578	35.44	0.9570	36.26	0.9610	31.09	0.9037	36.34	0.9642	37.13	0.9462
S4	30.18	0.8477	29.69	0.8667	29.45	0.8657	29.82	0.8755	26.25	0.7064	29.92	0.8779	32.26	0.8865
S5	27.25	0.8714	27.98	0.8897	27.74	0.8879	28.22	0.9062	24.34	0.7371	28.31	0.9073	29.29	0.8971
S6	32.82	0.9071	31.37	0.9019	30.91	0.9011	31.54	0.9125	26.70	0.7537	31.61	0.9140	34.00	0.9243
S7	28.69	0.8598	28.47	0.8745	28.29	0.8735	28.84	0.8929	25.05	0.7278	28.87	0.8924	30.95	0.8926
S8	29.57	0.9006	29.21	0.9060	28.74	0.9042	29.39	0.9186	24.25	0.7461	29.48	0.9191	30.93	0.9158
S9	33.61	0.9043	31.97	0.9002	31.74	0.9000	31.86	0.9018	28.45	0.7576	32.00	0.9063	34.78	0.9227
S10	35.41	0.9184	34.11	0.9260	32.55	0.9246	33.95	0.9314	25.12	0.7893	34.07	0.9332	34.05	0.9214
S11	29.72	0.9001	29.01	0.9086	28.62	0.9068	29.21	0.9219	24.45	0.7605	29.32	0.9229	31.26	0.9174
S12	29.21	0.8618	28.88	0.8733	28.62	0.8719	29.33	0.8936	25.36	0.7181	29.33	0.8922	31.31	0.8928
S13	26.63	0.8928	26.70	0.9068	26.23	0.9026	26.64	0.9154	21.76	0.7378	26.77	0.9164	28.46	0.9110
S14	28.18	0.8634	28.16	0.8761	27.98	0.8749	28.42	0.8910	24.67	0.7155	28.52	0.8918	30.34	0.8953
S15	30.62	0.8680	29.64	0.8671	29.42	0.8664	29.89	0.8812	26.25	0.7121	29.98	0.8817	32.48	0.8995
S16	29.45	0.8997	29.29	0.9069	29.03	0.9062	29.61	0.9189	25.17	0.7615	29.66	0.9202	31.30	0.9180
S17	28.24	0.8780	27.24	0.8660	26.96	0.8640	27.46	0.8863	23.70	0.7026	27.57	0.8860	29.92	0.8969
S18	26.15	0.8717	26.25	0.8826	25.95	0.8800	26.62	0.9014	22.19	0.7097	26.72	0.9013	28.20	0.8931
S19	33.66	0.9176	32.53	0.9177	32.12	0.9168	32.50	0.9213	27.98	0.7974	32.65	0.9253	34.49	0.9287
S20	33.03	0.8977	32.33	0.9011	31.81	0.9006	32.65	0.9153	27.50	0.7923	32.74	0.9175	34.34	0.9151
S21	31.79	0.8997	31.11	0.9077	30.70	0.9072	31.04	0.9100	26.43	0.7461	31.18	0.9137	33.18	0.9216
S22	32.30	0.9214	31.31	0.9192	30.99	0.9187	31.49	0.9303	27.35	0.8276	31.56	0.9322	33.86	0.9295
S23	33.47	0.9156	31.92	0.9117	31.49	0.9113	31.94	0.9172	27.40	0.7774	32.08	0.9208	34.42	0.9273
S24	31.09	0.9058	30.60	0.9073	30.30	0.9065	30.92	0.9205	26.75	0.7924	30.99	0.9226	32.75	0.9213
S25	27.27	0.8632	27.27	0.8745	26.95	0.8721	27.44	0.8968	23.33	0.7019	27.66	0.8966	29.25	0.8857
S26	34.62	0.8763	33.52	0.8831	33.05	0.8832	33.36	0.8817	29.85	0.7406	33.55	0.8885	35.74	0.9063
S27	33.65	0.9274	33.04	0.9217	32.36	0.9207	33.55	0.9380	27.27	0.8287	33.58	0.9393	34.73	0.9325
S28	29.99	0.8711	29.20	0.8689	28.94	0.8679	29.52	0.8893	25.70	0.7139	29.60	0.8891	31.73	0.8939
S29	32.02	0.9000	30.79	0.9022	30.23	0.9010	30.87	0.9101	26.02	0.7801	30.94	0.9122	33.38	0.9177
S30	33.61	0.9430	31.72	0.9270	31.22	0.9231	31.71	0.9362	26.88	0.8162	31.91	0.9403	33.97	0.9354
S31	27.66	0.8581	27.35	0.8700	27.14	0.8686	27.65	0.8889	23.93	0.7047	27.70	0.8879	29.87	0.8901
S32	26.09	0.8608	25.98	0.8731	25.81	0.8712	26.26	0.8930	22.53	0.6897	26.34	0.8923	28.33	0.8913
S33	27.71	0.8564	27.80	0.8690	27.61	0.8668	27.66	0.8773	23.78	0.6890	27.85	0.8791	29.70	0.8853
S34	29.22	0.8809	28.11	0.8873	27.82	0.8862	28.26	0.8979	24.06	0.6997	28.34	0.8984	31.00	0.9074
S35	30.26	0.9132	30.20	0.9145	29.71	0.9131	30.34	0.9236	25.15	0.7632	30.43	0.9252	31.53	0.9260
S36	25.32	0.8822	26.16	0.8902	25.77	0.8855	26.24	0.9117	22.35	0.7578	26.45	0.9123	27.63	0.8897
S37	29.62	0.9064	28.13	0.8924	27.79	0.8902	28.45	0.9102	23.84	0.7391	28.50	0.9098	30.99	0.9193
S38	30.03	0.8474	29.88	0.8645	29.86	0.8646	29.55	0.8593	27.31	0.6602	29.75	0.8650	32.00	0.8866
S39	29.06	0.8546	28.66	0.8622	28.42	0.8615	28.88	0.8764	25.10	0.6852	28.94	0.8761	31.09	0.8935
S40	30.61	0.9041	29.84	0.9019	29.43	0.9007	29.98	0.9122	25.33	0.7470	30.08	0.9139	32.15	0.9199
S41	27.69	0.8793	27.81	0.8867	27.54	0.8849	28.06	0.9028	23.92	0.7272	28.14	0.9032	29.61	0.9007
S42	31.06	0.9148	31.56	0.9189	30.97	0.9176	31.67	0.9283	26.67	0.8126	31.75	0.9301	32.56	0.9213
S43	32.92	0.9205	32.17	0.9187	31.80	0.9179	32.38	0.9275	28.08	0.8181	32.51	0.9309	34.29	0.9303
S44	31.09	0.9108	30.99	0.9095	30.23	0.9075	31.32	0.9281	24.93	0.7947	31.41	0.9272	32.03	0.9137
S45	37.08	0.9535	36.21	0.9537	34.69	0.9527	35.97	0.9557	28.30	0.8773	36.09	0.9588	36.13	0.9517
Avg	30.55	0.8920	29.97	0.8961	29.54	0.8946	30.12	0.9083	25.58	0.7531	30.23	0.9097	31.98	0.9102

TABLE IV
 QUANTITATIVE COMPARISON OF THE DIFFERENT SR METHODS ON THE DATASET (SCALE FACTOR $r=4$).

Scene	Bicubic		SRCNN		FSRCNN		VDSR		EDSR		DBPN		MA-GAN(3)	
	PSNR	SSIM	PSNR	SSIM	PSNR	SSIM	PSNR	SSIM	PSNR	SSIM	PSNR	SSIM	PSNR	SSIM
S1	19.72	0.5335	21.33	0.6073	21.24	0.6056	21.39	0.6222	19.13	0.4013	21.28	0.6379	23.11	0.6506
S2	27.21	0.7520	29.90	0.8178	29.64	0.8172	30.08	0.8314	24.30	0.6778	30.34	0.8493	30.64	0.8553
S3	32.03	0.8663	33.47	0.9003	33.10	0.9008	33.23	0.9025	28.30	0.8019	32.95	0.9079	35.40	0.9079
S4	24.88	0.5967	26.63	0.6832	26.53	0.6814	26.69	0.6883	23.66	0.5094	26.71	0.6993	26.54	0.7246
S5	21.36	0.6011	24.24	0.7236	24.10	0.7204	24.23	0.7308	21.10	0.4874	24.21	0.7449	26.81	0.7446
S6	26.33	0.6688	27.85	0.7405	27.69	0.7381	27.81	0.7462	23.92	0.5293	27.95	0.7639	29.16	0.7956
S7	23.37	0.6115	25.18	0.7119	25.06	0.7088	25.24	0.7208	22.12	0.5044	25.27	0.7361	26.32	0.7422
S8	22.96	0.6397	25.08	0.7372	24.92	0.7337	25.06	0.7428	20.93	0.4810	25.11	0.7584	25.42	0.7093
S9	27.61	0.6779	28.58	0.7372	28.51	0.7373	28.56	0.7403	25.79	0.5548	28.51	0.7467	29.83	0.7520
S10	29.02	0.7170	30.70	0.7891	30.33	0.7903	30.46	0.7905	22.40	0.5884	30.25	0.7959	31.69	0.8448
S11	23.31	0.6544	25.05	0.7521	24.87	0.7482	24.98	0.7577	20.99	0.5032	24.93	0.7709	25.83	0.7225
S12	23.59	0.6076	25.71	0.7057	25.57	0.7019	25.78	0.7143	22.50	0.4913	26.07	0.7383	26.56	0.7457
S13	20.45	0.6206	22.56	0.7350	22.40	0.7303	22.47	0.7369	18.31	0.4580	22.06	0.7376	23.13	0.6996
S14	22.57	0.6005	24.63	0.6977	24.53	0.6952	24.67	0.7053	21.69	0.4723	24.67	0.7191	25.45	0.6943
S15	24.99	0.6154	26.68	0.6984	26.58	0.6961	26.72	0.7050	23.59	0.5035	26.90	0.7238	27.77	0.7336
S16	23.36	0.6541	25.54	0.7512	25.41	0.7490	25.54	0.7566	22.02	0.5156	25.56	0.7692	27.94	0.7776
S17	21.92	0.6152	23.78	0.6873	23.65	0.6837	23.84	0.6985	20.74	0.4642	23.80	0.7150	26.53	0.7754
S18	19.93	0.5891	22.27	0.6984	22.10	0.6941	22.30	0.7082	18.83	0.4374	22.21	0.7218	23.68	0.7460
S19	27.45	0.7115	29.13	0.7854	28.99	0.7847	29.04	0.7867	25.19	0.6058	28.90	0.7906	30.88	0.8149
S20	27.09	0.7197	29.42	0.7850	29.22	0.7826	29.45	0.7945	24.93	0.6237	29.60	0.8130	29.33	0.7694
S21	25.59	0.6384	27.45	0.7378	27.33	0.7371	27.31	0.7355	23.65	0.4988	27.29	0.7411	28.54	0.7476
S22	26.65	0.7682	28.11	0.8196	27.92	0.8170	28.06	0.8259	24.47	0.6725	28.06	0.8366	30.75	0.8459
S23	27.15	0.7002	28.44	0.7653	28.32	0.7646	28.34	0.7664	24.58	0.5658	28.34	0.7759	29.12	0.7904
S24	25.19	0.7013	27.21	0.7790	27.08	0.7767	27.27	0.7866	23.75	0.6000	27.35	0.8008	29.35	0.8035
S25	21.12	0.5777	23.39	0.6800	23.26	0.6757	23.44	0.6918	20.49	0.4590	23.47	0.7124	25.98	0.7243
S26	29.14	0.6360	30.98	0.7089	30.84	0.7087	30.84	0.7076	28.12	0.5960	30.78	0.7130	31.38	0.7352
S27	27.56	0.7520	30.08	0.8223	29.85	0.8208	30.16	0.8325	24.58	0.6605	30.21	0.8469	29.61	0.7876
S28	24.13	0.6170	26.06	0.6871	25.95	0.6845	26.16	0.6974	23.19	0.5191	26.24	0.7158	27.58	0.7342
S29	26.29	0.7179	27.74	0.7696	27.56	0.7690	27.67	0.7741	23.13	0.6071	27.55	0.7806	29.02	0.8066
S30	25.99	0.7586	27.32	0.8002	27.06	0.7941	27.16	0.8052	22.83	0.5885	27.05	0.8139	29.02	0.8304
S31	22.15	0.6004	24.01	0.6939	23.91	0.6913	24.04	0.7029	21.07	0.4572	24.13	0.7211	25.23	0.7602
S32	20.30	0.5723	22.28	0.6812	22.14	0.6770	22.27	0.6887	19.40	0.4036	22.17	0.7023	23.22	0.7146
S33	21.77	0.5602	24.15	0.6680	24.10	0.6685	24.26	0.6806	20.73	0.4311	24.25	0.6953	23.72	0.7145
S34	23.13	0.6006	24.39	0.6922	24.24	0.6872	24.31	0.6940	21.00	0.4201	24.37	0.7111	27.96	0.7541
S35	23.45	0.6689	26.12	0.7523	25.95	0.7496	26.03	0.7554	21.85	0.5086	26.03	0.7673	25.85	0.7336
S36	19.50	0.6524	22.27	0.7446	22.09	0.7411	22.24	0.7601	19.41	0.5517	22.09	0.7772	22.54	0.6968
S37	22.87	0.6695	24.49	0.7321	24.34	0.7270	24.53	0.7401	20.44	0.4843	24.47	0.7565	26.90	0.7561
S38	24.57	0.5283	26.73	0.6347	26.71	0.6330	26.68	0.6345	24.99	0.4232	26.63	0.6403	27.54	0.6499
S39	23.39	0.5813	25.54	0.6748	25.40	0.6703	25.52	0.6806	22.54	0.4518	25.68	0.7049	26.20	0.7405
S40	24.36	0.6606	26.23	0.7377	26.11	0.7360	26.25	0.7447	22.32	0.5097	26.29	0.7587	27.99	0.7965
S41	21.59	0.6107	24.08	0.7162	23.94	0.7125	24.07	0.7235	20.65	0.4670	24.02	0.7371	27.33	0.7443
S42	25.13	0.7546	28.15	0.8047	27.93	0.8033	28.06	0.8097	23.80	0.6489	27.94	0.8192	26.29	0.8265
S43	26.83	0.7304	28.85	0.8043	28.73	0.8036	28.94	0.8121	24.93	0.6441	28.92	0.8216	29.07	0.7798
S44	24.39	0.7083	27.28	0.7876	27.01	0.7859	27.34	0.7993	21.92	0.6074	27.34	0.8155	29.10	0.8211
S45	30.07	0.8142	32.36	0.8695	31.98	0.8714	32.01	0.8692	24.76	0.7233	31.84	0.8753	31.67	0.8806
Avg	24.48	0.6585	26.48	0.7402	26.31	0.7379	26.46	0.7466	22.65	0.5358	26.44	0.7596	27.62	0.7640

TABLE V
 QUANTITATIVE COMPARISON OF THE DIFFERENT SR METHODS ON THE DATASET (SCALE FACTOR $r=8$).

Scene	Bicubic		SRCNN		FSRCNN		VDSR		EDSR		DBPN		MA-GAN(4)	
	PSNR	SSIM	PSNR	SSIM	PSNR	SSIM	PSNR	SSIM	PSNR	SSIM	PSNR	SSIM	PSNR	SSIM
S1	17.52	0.3522	19.27	0.3731	19.06	0.3795	19.34	0.3873	17.71	0.2986	19.19	0.4029	20.69	0.4250
S2	24.37	0.6217	26.69	0.6639	25.49	0.6692	26.87	0.6834	21.99	0.5903	27.03	0.7013	29.62	0.7586
S3	28.33	0.7773	30.04	0.7926	28.48	0.7895	30.11	0.8035	26.22	0.7316	30.13	0.8137	29.88	0.7787
S4	22.60	0.4542	24.24	0.4965	23.73	0.4951	24.25	0.5023	21.79	0.4059	24.15	0.5095	25.50	0.5325
S5	18.43	0.3721	21.28	0.4649	20.85	0.4734	21.31	0.4808	18.85	0.3303	20.96	0.4870	21.30	0.4412
S6	23.24	0.4714	24.96	0.5132	24.48	0.5154	25.01	0.5204	22.00	0.4031	24.80	0.5256	25.86	0.5335
S7	20.71	0.4255	22.36	0.4827	22.01	0.4853	22.41	0.4927	20.01	0.3671	22.18	0.4993	23.57	0.4966
S8	19.58	0.3966	21.63	0.4597	21.14	0.4638	21.65	0.4654	18.60	0.3103	21.26	0.4688	22.17	0.4547
S9	24.74	0.4978	26.19	0.5392	25.24	0.5334	26.15	0.5422	24.22	0.4411	25.94	0.5433	27.21	0.5573
S10	26.06	0.5682	27.94	0.6119	23.60	0.6014	27.94	0.6162	20.12	0.5014	27.79	0.6139	28.39	0.6271
S11	19.89	0.4222	21.54	0.4794	21.29	0.4895	21.62	0.4944	18.46	0.3363	21.30	0.5022	24.39	0.5220
S12	20.84	0.4154	22.91	0.4666	22.63	0.4743	23.04	0.4826	20.38	0.3574	23.05	0.5034	23.71	0.4869
S13	17.25	0.3719	19.43	0.4616	18.49	0.4613	19.32	0.4625	15.71	0.2736	18.78	0.4618	20.22	0.5358
S14	19.79	0.3907	21.88	0.4554	21.57	0.4557	21.85	0.4598	19.51	0.3199	21.49	0.4573	22.54	0.4619
S15	22.38	0.4420	24.18	0.4887	23.74	0.4915	24.25	0.4984	21.74	0.3885	24.18	0.5100	25.17	0.5169
S16	20.21	0.4267	22.35	0.4908	22.05	0.4961	22.40	0.4989	19.87	0.3625	22.10	0.5075	22.89	0.4818
S17	18.87	0.4017	21.07	0.4444	20.71	0.4561	21.14	0.4645	18.65	0.3292	20.85	0.4715	23.07	0.5120
S18	16.84	0.3613	18.95	0.4157	18.79	0.4230	18.99	0.4249	16.64	0.2714	18.71	0.4334	20.53	0.4894
S19	24.44	0.5449	26.18	0.5895	25.05	0.5913	26.24	0.6007	22.91	0.4870	26.02	0.6036	27.78	0.6290
S20	24.08	0.5774	26.41	0.6018	25.86	0.6118	26.56	0.6205	22.91	0.5286	26.72	0.6481	28.53	0.6608
S21	22.58	0.4159	24.67	0.4947	24.09	0.4917	24.63	0.4927	21.68	0.3555	24.23	0.4829	25.21	0.4877
S22	23.78	0.6420	25.09	0.6484	24.35	0.6553	25.28	0.6713	22.24	0.5742	25.21	0.6919	27.63	0.7302
S23	24.10	0.5203	25.51	0.5472	24.78	0.5499	25.54	0.5538	22.53	0.4377	25.27	0.5546	26.57	0.5764
S24	22.20	0.5272	24.20	0.5738	23.69	0.5818	24.31	0.5899	21.69	0.4833	24.20	0.6047	26.46	0.6281
S25	18.57	0.3737	20.71	0.4291	20.51	0.4382	20.80	0.4465	18.56	0.3293	20.62	0.4589	22.22	0.4739
S26	27.24	0.5353	29.50	0.5842	28.51	0.5783	29.47	0.5849	27.83	0.5443	29.48	0.5882	30.09	0.6186
S27	24.28	0.5935	26.61	0.6397	25.96	0.6556	26.88	0.6681	22.02	0.5639	26.97	0.6918	26.84	0.6371
S28	21.56	0.4588	23.74	0.4979	23.31	0.5017	23.83	0.5107	21.43	0.4221	23.75	0.5220	24.41	0.5243
S29	23.28	0.5826	25.00	0.6017	23.78	0.6009	25.06	0.6124	20.92	0.5152	24.84	0.6185	25.90	0.6304
S30	21.75	0.5534	23.38	0.5476	22.43	0.5588	23.56	0.5786	20.03	0.4332	23.18	0.5967	24.30	0.5926
S31	19.40	0.3890	21.33	0.4370	21.04	0.4417	21.36	0.4470	19.12	0.3099	21.08	0.4510	22.24	0.4584
S32	17.43	0.3227	19.41	0.3899	19.14	0.3936	19.40	0.3937	17.36	0.2288	18.94	0.3910	20.30	0.3936
S33	18.81	0.3378	21.36	0.4184	20.80	0.4208	21.27	0.4233	18.55	0.2783	21.07	0.4440	21.66	0.4141
S34	20.17	0.3673	21.57	0.4071	21.22	0.4078	21.63	0.4101	19.19	0.2743	21.33	0.4164	22.99	0.4377
S35	19.95	0.4260	22.82	0.4959	22.24	0.4960	22.78	0.4986	19.37	0.3468	22.36	0.4948	23.08	0.5070
S36	16.77	0.4675	19.43	0.5058	19.16	0.5261	19.54	0.5410	17.49	0.4392	19.29	0.5716	19.85	0.5051
S37	19.23	0.4341	21.03	0.4648	20.83	0.4747	21.17	0.4808	17.85	0.3264	20.94	0.4945	21.81	0.4846
S38	22.42	0.3352	25.09	0.4150	24.04	0.4062	25.02	0.4113	23.84	0.3111	24.84	0.4104	25.38	0.4291
S39	20.75	0.3768	22.99	0.4370	22.61	0.4380	23.05	0.4422	20.78	0.3211	22.89	0.4564	23.58	0.4508
S40	21.13	0.4392	23.25	0.4895	22.74	0.4899	23.29	0.4953	20.34	0.3720	23.00	0.5026	23.85	0.5032
S41	18.64	0.3863	21.01	0.4515	20.66	0.4576	21.04	0.4635	18.41	0.3082	20.65	0.4680	21.82	0.4986
S42	22.28	0.6301	25.11	0.6387	24.35	0.6414	25.22	0.6542	21.66	0.5609	24.94	0.6658	25.99	0.7007
S43	23.66	0.5652	25.45	0.6157	24.91	0.6214	25.59	0.6321	22.69	0.5330	25.50	0.6471	26.14	0.6021
S44	20.86	0.5394	23.89	0.6033	22.77	0.6068	24.00	0.6222	19.77	0.5142	23.88	0.6334	25.28	0.6502
S45	25.94	0.6612	28.46	0.7274	25.64	0.7199	28.04	0.7285	21.46	0.6002	27.62	0.7218	27.84	0.6904
Avg	21.49	0.4705	23.56	0.5190	22.84	0.5225	23.60	0.5301	20.56	0.4093	23.39	0.5387	24.54	0.5450

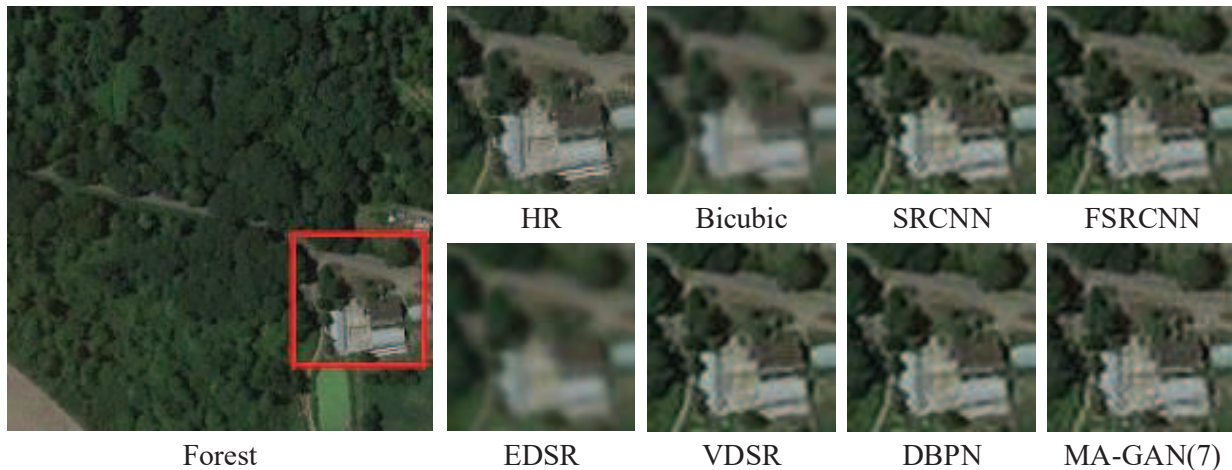


Fig. 5. Visual comparisons between MA-GAN and other methods (scale factor $r=2$).

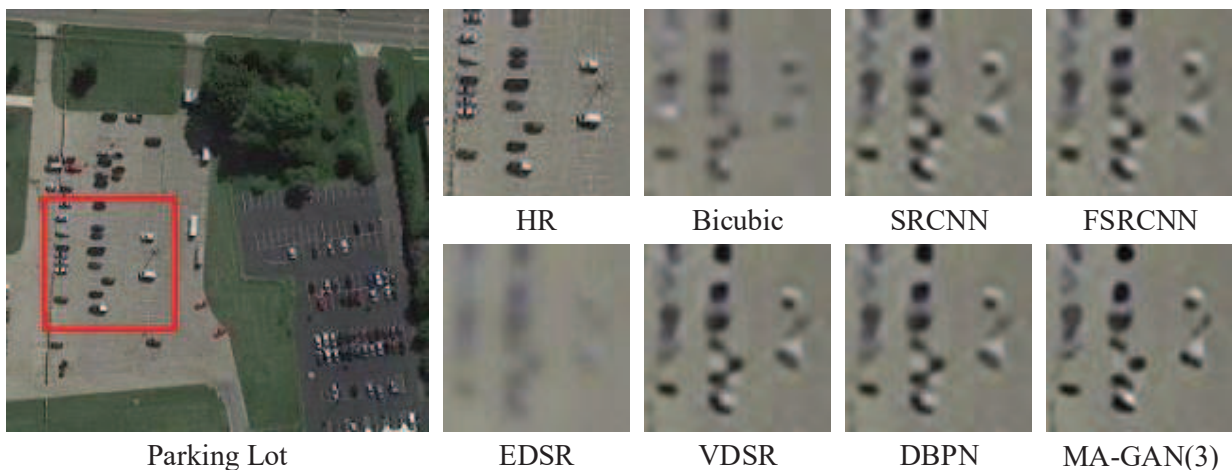


Fig. 6. Visual comparisons between MA-GAN and other methods (scale factor $r=4$).

obtains the highest SSIM value for 34 scenes and is lower than only DBPN in all other 11 scenes. The last one is the case of $r = 8$ (Table V), where MA-GAN(4) achieves the highest average PSNR of 24.54 dB and the average SSIM of 0.5450. The PSNR of MA-GAN(4) is 0.98 dB higher than the second-best result, while the SSIM is 0.0063 higher. MA-GAN(4) performs better in PSNR than almost all other methods and is not ranked first in only 4 scenes. With respect to SSIM, MA-GAM(7) performs better on 29 scenes.

In summary, our MA-GAN outperforms all the other methods for $r = 2, 4, 8$, respectively. In particular, MA-GAN is basically more than 1 dB higher than the second-best results among all methods in terms of PSNR values, with a maximum difference of 1.43 dB. However, the lead is not as large in SSIM. The result is only 0.0005 higher than DBPN at $r = 2$. This is probably because the SR task of upsampling by a scale factor of 2 is simpler and the gap is not significant in this aspect. When r increases, the advantage of MA-GAN in SSIM becomes more obvious, with a maximum improvement of 0.0063 over the second-place condition ($r = 8$). Overall, although there are still some unsatisfactory aspects, our MA-GAN still performs the best.

V. CONCLUSION

In this paper, we present a GAN-based SR network named the multi-attention-GAN that correctly learns the mapping from LR to HR images to generate perceptually pleasing HR images. Specifically, we first designed a GAN-based framework for the image SR task. The key to accomplishing the SR task is the image generator with post-upsampling that we designed. The main body of the generator contains two blocks; one is the PCRDB block, and the other is the AUP block. The AttPConv in the PCRDB block is a module that combines multi-scale convolution and channel attention to automatically learn and adjust the scaling of the residuals for better results. The AUP block is a module that combines pixel attention to perform arbitrary multiples of upsampling. These two blocks work together to help generate better quality images. For the loss function, we design a loss function based on pixel loss and introduce both adversarial loss and feature loss to guide the generator learning. Finally, it is demonstrated by our experiments that our proposed MA-GAN can perform better than some state-of-the-art SR methods.

Our MA-GAN still encounters difficulty in generating tiny textures, which is a problem for all super-resolution algo-

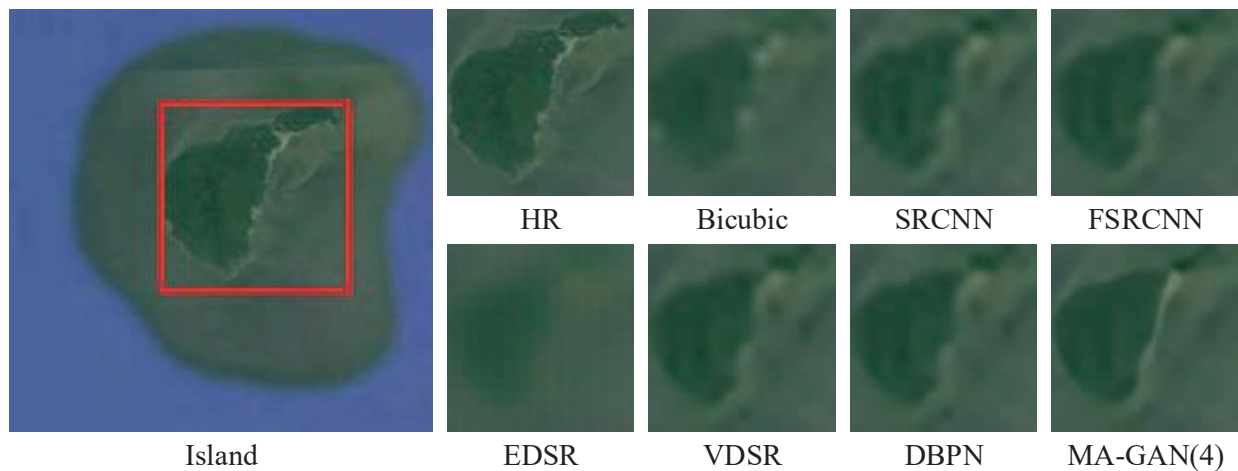


Fig. 7. Visual comparisons between MA-GAN and other methods (scale factor $r=8$).

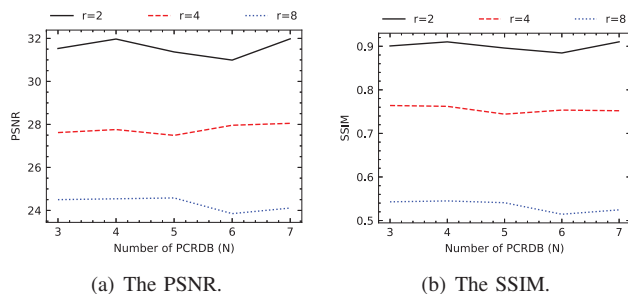


Fig. 8. The comparison results when MA-GAN contains different numbers of PCRDD blocks.

rithms, and we will continue to work on this issue in the future. Additionally, inspired by the satisfactory performance of our model, we will attempt to integrate our SR models into other vision tasks to help improve the results.

REFERENCES

- [1] J. S. Isaac and R. Kulkarni, "Super resolution techniques for medical image processing," in *2015 International Conference on Technologies for Sustainable Development (ICTSD)*. IEEE, 2015, pp. 1–6.
- [2] H. Greenspan, "Super-resolution in medical imaging," *The computer journal*, vol. 52, no. 1, pp. 43–63, 2009.
- [3] Y. Huang, L. Shao, and A. F. Frangi, "Simultaneous super-resolution and cross-modality synthesis of 3d medical images using weakly-supervised joint convolutional sparse coding," in *Proceedings of the IEEE Conference on Computer Vision and Pattern Recognition*, 2017, pp. 6070–6079.
- [4] K. Li, Y. Zhu, J. Yang, and J. Jiang, "Video super-resolution using an adaptive superpixel-guided auto-regressive model," *Pattern Recognition*, vol. 51, pp. 59–71, 2016.
- [5] J. Caballero, C. Ledig, A. Aitken, A. Acosta, J. Totz, Z. Wang, and W. Shi, "Real-time video super-resolution with spatio-temporal networks and motion compensation," in *Proceedings of the IEEE Conference on Computer Vision and Pattern Recognition*, 2017, pp. 4778–4787.
- [6] P. Rasti, T. Uiboupin, S. Escalera, and G. Anbarjafari, "Convolutional neural network super resolution for face recognition in surveillance monitoring," in *International conference on articulated motion and deformable objects*. Springer, 2016, pp. 175–184.
- [7] W. W. Zou and P. C. Yuen, "Very low resolution face recognition problem," *IEEE Transactions on image processing*, vol. 21, no. 1, pp. 327–340, 2011.
- [8] Y. Bai, Y. Zhang, M. Ding, and B. Ghanem, "Sod-mtgan: Small object detection via multi-task generative adversarial network," in *Proceedings of the European Conference on Computer Vision (ECCV)*, 2018, pp. 206–221.
- [9] Z. Zou and Z. Shi, "Ship detection in spaceborne optical image with svd networks," *IEEE Transactions on Geoscience and Remote Sensing*, vol. 54, no. 10, pp. 5832–5845, 2016.
- [10] A. J. Tatem, H. G. Lewis, P. M. Atkinson, and M. S. Nixon, "Super-resolution target identification from remotely sensed images using a hopfield neural network," *IEEE Transactions on Geoscience and Remote Sensing*, vol. 39, no. 4, pp. 781–796, 2001.
- [11] J. Cheng, Q. Kuang, C. Shen, J. Liu, X. Tan, and W. Liu, "Reslap: Generating high-resolution climate prediction through image super-resolution," *IEEE Access*, vol. 8, pp. 39 623–39 634, 2020.
- [12] A. Elfadaly, W. Attia, and R. Lasaponara, "Monitoring the environmental risks around medinet habu and ramesseum temple at west luxor, egypt, using remote sensing and gis techniques," *Journal of Archaeological Method and Theory*, vol. 25, no. 2, pp. 587–610, 2018.
- [13] Z. Liu, G. Li, G. Mercier, Y. He, and Q. Pan, "Change detection in heterogeneous remote sensing images via homogeneous pixel transformation," *IEEE Transactions on Image Processing*, vol. 27, no. 4, pp. 1822–1834, 2017.
- [14] Z. Shi and Z. Zou, "Can a machine generate humanlike language descriptions for a remote sensing image?" *IEEE Transactions on Geoscience and Remote Sensing*, vol. 55, no. 6, pp. 3623–3634, 2017.
- [15] Y. Yu, X. Li, and F. Liu, "E-dbpn: Enhanced deep back-projection networks for remote sensing scene image superresolution," *IEEE Transactions on Geoscience and Remote Sensing*, 2020.
- [16] D. Zhang, J. Shao, X. Li, and H. T. Shen, "Remote sensing image super-resolution via mixed high-order attention network," *IEEE Transactions on Geoscience and Remote Sensing*, 2020.
- [17] R. Keys, "Cubic convolution interpolation for digital image processing," *IEEE transactions on acoustics, speech, and signal processing*, vol. 29, no. 6, pp. 1153–1160, 1981.
- [18] C. E. Duchon, "Lanczos filtering in one and two dimensions," *Journal of applied meteorology*, vol. 18, no. 8, pp. 1016–1022, 1979.
- [19] J. Sun, Z. Xu, and H.-Y. Shum, "Image super-resolution using gradient profile prior," in *2008 IEEE Conference on Computer Vision and Pattern Recognition*. IEEE, 2008, pp. 1–8.
- [20] Y.-W. Tai, S. Liu, M. S. Brown, and S. Lin, "Super resolution using edge prior and single image detail synthesis," in *2010 IEEE computer society conference on computer vision and pattern recognition*. IEEE, 2010, pp. 2400–2407.
- [21] C.-Y. Yang, J.-B. Huang, and M.-H. Yang, "Exploiting self-similarities for single frame super-resolution," in *Asian conference on computer vision*. Springer, 2010, pp. 497–510.
- [22] W. Dong, F. Fu, G. Shi, X. Cao, J. Wu, G. Li, and X. Li, "Hyperspectral image super-resolution via non-negative structured sparse representation," *IEEE Transactions on Image Processing*, vol. 25, no. 5, pp. 2337–2352, 2016.
- [23] X. Lu, Y. Yuan, and P. Yan, "Image super-resolution via double

- sparsity regularized manifold learning,” *IEEE transactions on circuits and systems for video technology*, vol. 23, no. 12, pp. 2022–2033, 2013.
- [24] C. Dong, C. C. Loy, K. He, and X. Tang, “Learning a deep convolutional network for image super-resolution,” in *European conference on computer vision*. Springer, 2014, pp. 184–199.
- [25] K. He, X. Zhang, S. Ren, and J. Sun, “Deep residual learning for image recognition,” in *Proceedings of the IEEE conference on computer vision and pattern recognition*, 2016, pp. 770–778.
- [26] G. Huang, Z. Liu, L. Van Der Maaten, and K. Q. Weinberger, “Densely connected convolutional networks,” in *Proceedings of the IEEE conference on computer vision and pattern recognition*, 2017, pp. 4700–4708.
- [27] J. Kim, J. Kwon Lee, and K. Mu Lee, “Accurate image super-resolution using very deep convolutional networks,” in *Proceedings of the IEEE conference on computer vision and pattern recognition*, 2016, pp. 1646–1654.
- [28] B. Lim, S. Son, H. Kim, S. Nah, and K. Mu Lee, “Enhanced deep residual networks for single image super-resolution,” in *Proceedings of the IEEE conference on computer vision and pattern recognition workshops*, 2017, pp. 136–144.
- [29] M. Haris, G. Shakhnarovich, and N. Ukita, “Deep back-projection networks for super-resolution,” in *Proceedings of the IEEE conference on computer vision and pattern recognition*, 2018, pp. 1664–1673.
- [30] S. Zhang, Q. Yuan, J. Li, J. Sun, and X. Zhang, “Scene-adaptive remote sensing image super-resolution using a multiscale attention network,” *IEEE Transactions on Geoscience and Remote Sensing*, 2020.
- [31] I. Goodfellow, J. Pouget-Abadie, M. Mirza, B. Xu, D. Warde-Farley, S. Ozair, A. Courville, and Y. Bengio, “Generative adversarial nets,” in *Advances in neural information processing systems*, 2014, pp. 2672–2680.
- [32] X. Wang, K. Yu, S. Wu, J. Gu, Y. Liu, C. Dong, Y. Qiao, and C. Change Loy, “Esrgan: Enhanced super-resolution generative adversarial networks,” in *Proceedings of the European Conference on Computer Vision (ECCV) Workshops*, 2018, pp. 0–0.
- [33] Y. Zhang, K. Li, K. Li, L. Wang, B. Zhong, and Y. Fu, “Image super-resolution using very deep residual channel attention networks,” in *Proceedings of the European Conference on Computer Vision (ECCV)*, 2018, pp. 286–301.
- [34] H. Zhao, X. Kong, J. He, Y. Qiao, and C. Dong, “Efficient image super-resolution using pixel attention,” *arXiv preprint arXiv:2010.01073*, 2020.
- [35] W. Shi, J. Caballero, F. Huszár, J. Totz, A. P. Aitken, R. Bishop, D. Rueckert, and Z. Wang, “Real-time single image and video super-resolution using an efficient sub-pixel convolutional neural network,” in *Proceedings of the IEEE conference on computer vision and pattern recognition*, 2016, pp. 1874–1883.
- [36] C. Dong, C. C. Loy, K. He, and X. Tang, “Image super-resolution using deep convolutional networks,” *IEEE transactions on pattern analysis and machine intelligence*, vol. 38, no. 2, pp. 295–307, 2015.
- [37] C. Ledig, L. Theis, F. Huszár, J. Caballero, A. Cunningham, A. Acosta, A. Aitken, A. Tejani, J. Totz, Z. Wang *et al.*, “Photo-realistic single image super-resolution using a generative adversarial network,” in *Proceedings of the IEEE conference on computer vision and pattern recognition*, 2017, pp. 4681–4690.
- [38] W.-S. Lai, J.-B. Huang, N. Ahuja, and M.-H. Yang, “Deep laplacian pyramid networks for fast and accurate super-resolution,” in *Proceedings of the IEEE conference on computer vision and pattern recognition*, 2017, pp. 624–632.
- [39] L. Gatys, A. S. Ecker, and M. Bethge, “Texture synthesis using convolutional neural networks,” in *Advances in neural information processing systems*, 2015, pp. 262–270.
- [40] Y. Yuan, S. Liu, J. Zhang, Y. Zhang, C. Dong, and L. Lin, “Unsupervised image super-resolution using cycle-in-cycle generative adversarial networks,” in *Proceedings of the IEEE Conference on Computer Vision and Pattern Recognition Workshops*, 2018, pp. 701–710.
- [41] I. C. Duta, L. Liu, F. Zhu, and L. Shao, “Pyramidal convolution: Rethinking convolutional neural networks for visual recognition,” *arXiv preprint arXiv:2006.11538*, 2020.
- [42] C. Szegedy, S. Ioffe, V. Vanhoucke, and A. Alemi, “Inception-v4, inception-resnet and the impact of residual connections on learning,” in *Proceedings of the AAAI Conference on Artificial Intelligence*, vol. 31, no. 1, 2017.
- [43] G. Cheng, J. Han, and X. Lu, “Remote sensing image scene classification: Benchmark and state of the art,” *Proceedings of the IEEE*, vol. 105, no. 10, pp. 1865–1883, 2017.
- [44] D. P. Kingma and J. Ba, “Adam: A method for stochastic optimization,” *arXiv preprint arXiv:1412.6980*, 2014.
- [45] C. Dong, C. C. Loy, and X. Tang, “Accelerating the super-resolution convolutional neural network,” in *European conference on computer vision*. Springer, 2016, pp. 391–407.